Unveiling the origins of quasi-phase matching spectral imperfections in thin-film lithium niobate frequency doublers

Jie Zhao,[1, a)] Xiaoting Li,[2, a)] Ting-Chen Hu,[1] Ayed Al Sayem,[1] Haochuan Li,[2] Alaric Tate,[1] Kwangwoong Kim,[1] Rose Kopf,[1] Pouria Sanjari,[1, b)] Mark Earnshaw,[1] Nicolas K. Fontaine,[1] Cheng Wang,[2] and Andrea Blanco-Redondo[1, c)]

[1)]*Nokia Bell Labs, 600 Mountain Avenue, Murray Hill, NJ 07974, USA*

[2)]*Department of Electrical Engineering & State Key Laboratory of Terahertz and Millimeter Waves, City University of Hong Kong, Hong Kong, China*

(*Electronic mail: jie.2.zhao@nokia-bell-labs.com.)

(Dated: 27 October 2023)

Thin-film lithium niobate (TFLN) based frequency doublers have been widely recognized as essential components for both classical and quantum optical communications. Nonetheless, the efficiency (unit: %/W) of these devices is hindered by imperfections present in the quasi-phase matching (QPM) spectrum. In this report, we present a thorough experimental study of the spectral imperfections in TFLN frequency doublers with varying lengths, ranging from 5 mm to 15 mm. A non-destructive diagnostic method based on scattered light imaging is proposed and employed to identify the waveguide sections and primary waveguide parameters contributing to the imperfections in the QPM spectrum. By applying this method, we obtain the evolution of the QPM spectrum along the waveguide's length. Correlating this information with measurements of the relevant geometric parameters along the waveguides suggests that TFLN film thickness variation is the primary source for the measured spectral distortions. Furthermore, we numerically reproduce the QPM spectra with the mapped TFLN film thickness across the entire waveguiding regions. These findings align with and complement the simulation results from previous numerical studies, providing further evidence of the effectiveness of the developed diagnostic method. This comprehensive investigation offers valuable insights into the identification and mitigation of spectral imperfections in TFLN-based frequency doublers, paving the way toward the realization of nonlinear optical devices with enhanced efficiency and improved spectral fidelity.

I. INTRODUCTION

Thin-film periodically poled lithium niobate (PPLN) waveguides offer a compelling platform for achieving highly efficient wavelength conversion devices, leveraging their high second-order nonlinear coefficient ($\chi^{(2)}$) and tight confinement of optical modes. These waveguides have found diverse applications in second-harmonic generation (SHG)[1–8], entangled photon-pair generation[9,10], optical parametric amplification[11], optical isolation[12], and all-optical switching[13]. However, compared to their bulk counterparts, these waveguides exhibit an increased susceptibility to fabrication inhomogeneities, presenting a significant challenge to their overall performance[4,14,15]. These inhomogeneities can give rise to unfavorable effects in the QPM spectrum, including broadened central peaks and unwanted side lobes, resulting in reduced conversion efficiency. Furthermore, as phase errors accumulate along the waveguide's length, longer devices experience more pronounced impacts from fabrication non-uniformity, hindering further enhancements of their power conversion efficiency (unit: %/W)[16]. To date, the demonstrated thin-film PPLN devices have typically had lengths ranging between 4 and 6 mm. As a result, even though these thin-film devices exhibit length-normalized conversion efficiencies (unit: %/W/cm^2) more than 20 times higher than their bulk counterparts[1,4–6], their power conversion efficiencies (unit: %/W) remain lower than the reported values from the state-of-the-art bulk devices[17,18]. Therefore, it is imperative to direct research efforts towards investigating approaches that can enable the fabrication of longer thin-film PPLN devices while ensuring good spectral fidelity. This will help bridge the performance gap with bulk LN devices and unlock the full potential of thin-film PPLN technology.

Prominent studies have examined the impact of fabrication inhomogeneities on the QPM spectrum from Ti-indiffused and diced Zn-indiffused bulk lithium niobate (LN) waveguides[19–21], with a specific focus on waveguide width variation as the primary error source. In particular, in Ref. [19], 83 mm Ti-indiffused PPLN waveguides were diced into shorter sections to analyze the generated QPM spectra from different regions of the waveguides, thereby revealing the evolution of the QPM spectrum along the waveguide's length. In addition, through the usage of aperiodically poled bulk LN waveguides and frequency-resolved optical gating, Chang et al. successfully obtained the complex transfer function of the SHG process and thus were able to infer the related fabrication errors[22]. In the context of thin-film PPLN devices, numerical studies have been reported to estimate sensitivity of the QPM spectrum to various waveguide parameters, with efforts also made to replicate the measured QPM spectrum based on estimated TFLN film thickness profiles[14,15,23,24]. However, comprehensive experimental investigations akin to those described in Ref. [19] for bulk LN waveguides, are currently lacking for thin-film PPLN devices.

[a)]These authors contributed equally to this work.

[b)]Also at Department of Electrical & Systems Engineering, University of Pennsylvania, Philadelphia, PA 19104, USA

[c)]Also at CREOL, The College of Optics and Photonics, University of Central Florida, Orlando, FL 32816, USA

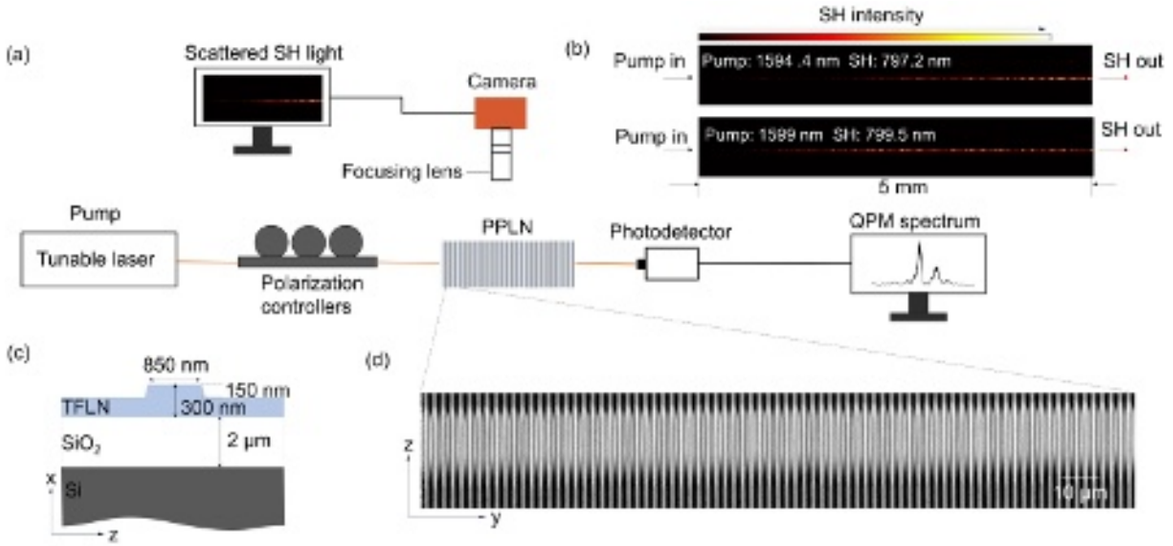

FIG. 1. (a) Schematic of the experimental setup for SHG characterization. (b) Images of the collected scattered SH light from a 5 mm long PPLN waveguide with the pump wavelength at 1594.4 nm and 1599 nm respectively. (c) Cross section of the PPLN waveguides. (d) Second-harmonic microscope image of the periodically poled lithium niobate thin film.

Here, we introduce a non-destructive optical diagnostic method that enables visualization of the QPM spectrum at any location along the thin-film PPLN waveguide. This approach is applicable to various types of thin-film PPLN waveguides and requires a simple experimental apparatus with only minor modifications to the traditional SHG characterization setup (as illustrated in Fig. 1(a)). To accomplish this, we utilize a monochrome camera positioned perpendicular to the chip surface to capture the scattered second-harmonic (SH) light across the entire PPLN waveguiding region. By acquiring multiple images while sweeping the pump wavelengths, the local QPM spectra at different locations on the waveguide can subsequently be calculated and obtained. This technique uncovers the contributions from different sections of the waveguide to the final QPM spectrum, facilitating an in-depth understanding of the imperfections observed in the measured spectra. To evaluate the efficacy of our approach, we conducted investigations on thin-film PPLN waveguides with lengths of 5 mm, 7.5 mm, 12.5 mm, and 15 mm. Our findings indicate that the observed imperfections in the spectra primarily stem from variations in TFLN film thickness. Subsequently, we mapped the film thickness across the entire waveguiding regions. This mapping allowed us to numerically reproduce the measured QPM spectra, further confirming the significant influence of film thickness variations on the spectral imperfections and the effectiveness of the diagnostic approach introduced in this study.

II. METHODS

The thin-film PPLN waveguides were fabricated using 5 mol% MgO-doped 300 nm x-cut lithium niobate on insulator (LNOI) wafers. In this report, all measured waveguides have a targeted etching depth of 150 nm and a waveguide top width of approximately 850 nm, as shown in Fig. 1(c). These waveguides were designed for efficient SHG from telecommunication wavelengths to near-visible wavelengths. The required poling period for QPM is about 2.46 μm, and all the interacting waves are in the fundamental TE mode.

In the initial fabrication step, poling electrodes with lengths varying from 5 mm to 15 mm were formed on the surface of TFLN using photolithography, while maintaining a fixed poling period of 2.46 μm for each electrode. High-voltage pulses, as described in Ref. [25], were then applied to these electrodes for periodic poling of the TFLN. To assess the fidelity of the fabricated domains, multiple SH microscope images were generated at different locations along each waveguide. Figure 1(d) presents a representative SH microscope image of the poled area, revealing domain structures with ideal uniformity and duty cycles, which are crucial for efficient frequency conversion. It is worth emphasizing that achieving high-fidelity poling of TFLN with long lengths and small periods has been challenging. As the poling periods decrease, adjacent domains tend to merge, while longer waveguides introduce greater variations in the duty cycle. Here, even for the 15 mm long poling electrodes, the calculated poling duty cycle remains highly uniform, at 52.83% $\pm$ 2.28%. Therefore, contributions from imperfect periodic poling of TFLN (as discussed in detail through theoretical calculations in Ref. [26]) to the QPM spectra are not considered in our subsequent discussions and numerical simulations. The waveguides were fabricated in the poled areas through aligned electron beam lithography and dry etching, followed by a wet etching process for sidewall deposition cleaning. Finally, the chip edges were cleaved to ensure optimal edge coupling.

The experimental setup for SHG characterization is depicted in Fig. 1(a). A tunable laser operating at telecommu-

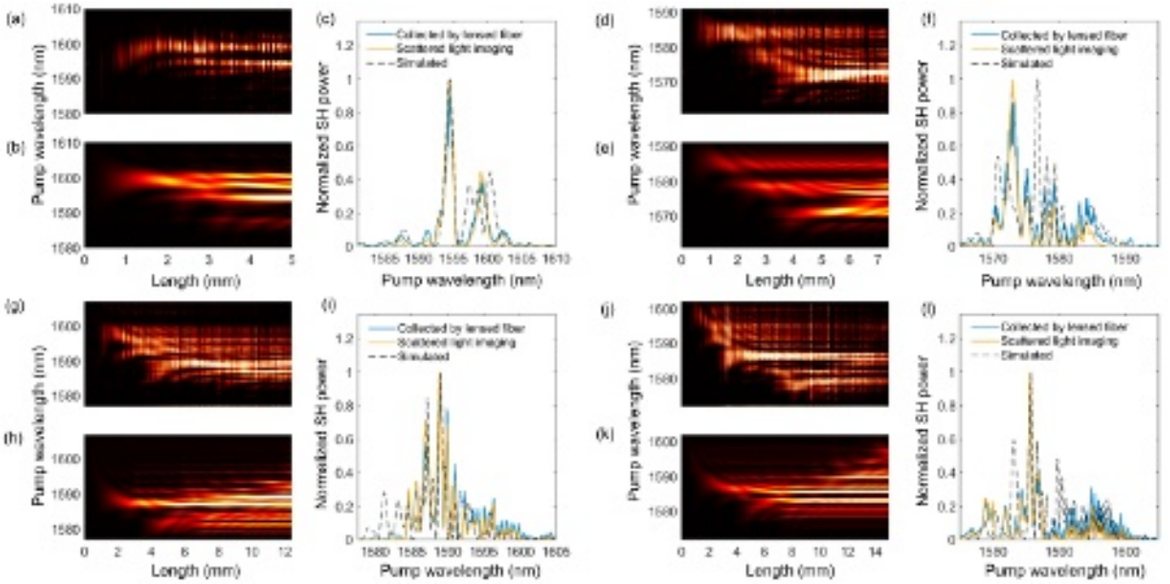

FIG. 2. Measured and simulated QPM spectrum mappings and end-point QPM spectra from thin-film PPLN waveguides with different lengths of 5 mm (a)-(c), 7.5 mm (d)-(f), 12.5 mm (g)-(i), and 15 mm (j)-(l). (a), (d), (g), and (j): Measured QPM spectrum mappings using scattered-light imaging. (b), (e), (h), and (k): Calculated QPM spectrum mappings based on measured TFLN film thickness profiles. (c), (f), (i), and (l): Measured end-point QPM spectra using the conventional method (blue curves), as well as scattered-light imaging (yellow curves), overlaid with calculated plots (dashed black curves) based on TFLN film thickness profiles.

nication wavelengths serves as the pump source for the PPLN waveguides, with its polarization adjusted by a set of polarization controllers to ensure TE mode injection at the waveguide's input facet. Light is coupled into and out of the chip using tapered lensed fibers to optimize the coupling efficiency. While sweeping the pump wavelength, the corresponding SH light is collected at the output waveguide facet using a lensed fiber and detected by a Si photodetector, following the conventional method for obtaining the QPM spectrum. Additionally, we developed and employed a second approach for SHG characterization, which not only provides QPM spectrum information at any location along the waveguide but also facilitates the identification of sources causing spectral imperfections. Specifically, while sweeping the pump wavelengths, a monochrome camera (Allied Vision Alvium 1800 U-511) was used to image the scattered SH light along the waveguide region. For example, Fig. 1(b) presents the measured scattered SH light images from a 5 mm thin-film PPLN waveguide with pump wavelengths of 1594.4 nm and 1599 nm, respectively. As we can see in these images, SH light with different wavelengths is scattered from distinct parts of the waveguide. In the case of this waveguide, the 799.5 nm SH light forms an unwanted side lobe in the QPM spectrum, and Fig. 1(b) indicates that it is primarily generated near the initial section of the PPLN. Such information proves valuable for comprehending and addressing QPM spectral imperfections, particularly in longer waveguides, as further elaborated in the subsequent sections.

III. RESULTS

We measured SHG from PPLN waveguides with lengths of 5 mm, 7.5 mm, 12.5 mm, and 15 mm. Note that these waveguides are located on the same chip, sharing an identical total length of approximately 18 mm, with their input and output ports extending to the edges of the chip. Their relative positions are indicated in Fig. 3(a), with the black lines showing the locations and the lengths of the periodically poled regions, which are the concerned regions for the subsequent QPM spectra analysis. The QPM spectra obtained by the conventional method (as described in the previous paragraph) are shown as the blue curves in Figs. 2(c), (f), (i), and (l). Upon comparing these plots, it becomes evident that increasing the waveguide length leads to the generation of more side lobes, thereby diminishing the spectrum fidelity and the overall achievable conversion efficiency. The variations in the main peak wavelengths can be attributed to a combination of slight differences in the designed waveguide widths and the film thicknesses from one waveguide to another, as illustrated in Fig. 3(b). The spectrum fidelity values (F), calculated using the definition from Ref. [16], are 0.46, 0.24, 0.17, and 0.15 respectively for the four lengths. To gain deeper insights into the origins of these side lobes, we captured scattered SH light images for each waveguide while sweeping the pump wavelengths, similar to the representative images shown in Fig. 1(b). By integrating the pixel values in each column of these images (perpendicular to the waveguide's direction), we obtained mappings of the SH light in terms of propagation length and pump wavelength, which

are presented as color images in Figs. 2(a), (d), (g), and (j). These visual representations conveniently illustrate the evolution of the QPM spectrum along the waveguide. Moreover, end-point QPM spectra, which correspond to the QPM spectra obtained at the end of the PPLN waveguides, can be generated by averaging the final column values of the SH light mappings. The purpose of this averaging process is to smooth out the non-uniformity present in the measured scattered SH light along the length of the waveguide, which is likely attributed to speckle patterns/noise generated by the interference among scattered coherent SH light originating from various locations on the waveguide. This averaging process proves effective for the scope of this study, ensuring that the non-uniformity in the scattered SH light does not impact the discussion and analysis presented here. The generated QPM spectra are depicted by the yellow curves in Figs. 2(c), (f), (i), and (l). The close alignment between these curves and QPM spectra obtained through the conventional method provides compelling evidence that valid QPM spectra can be obtained using the scattered light imaging technique at any location along the PPLN waveguide. Therefore, we analyze imperfections in the QPM spectra based on the SH light mappings. Notably, these mappings exhibit a consistent trend: side peaks with longer wavelengths than the main peaks predominantly arise from the initial section of the waveguides, while the SH light from the main peaks only begins to emerge at approximately 2-3 mm away from the waveguides' starting points. This similarity suggests the presence of one or several waveguide geometry parameters that consistently vary along the direction of light propagation across the entire chip.

For uniform waveguides, the QPM spectrum (Φ, normalized per unit length) can be calculated as[15,16]:

$$\begin{aligned} \Phi &= \mathrm{sinc}(\frac{\Delta\beta L}{2})\exp(i\frac{\Delta\beta L}{2}), \\ \Delta\beta &= \frac{2\pi}{\lambda_{\mathrm{SH}}}n_{\mathrm{SH}} - 2\frac{2\pi}{\lambda_{\mathrm{pump}}}n_{\mathrm{pump}} - \frac{2\pi}{\Lambda}, \end{aligned} \tag{1}$$

where L is the length of the waveguide, $\lambda_{\mathrm{pump,\,SH}}$ denotes the pump and SH wavelengths, and $n_{\mathrm{pump,\,SH}}$ indicates the effective mode indices for the pump and SH light. To determine the type of fabrication errors causing these spectrum imperfections, we calculated partial derivatives of the momentum mismatch ($\Delta\beta$, as defined in Eq. 1) with respect to waveguide top width w, etching depth h_{etch}, and film thickness t_{LN} as follows:

$$\begin{aligned} &(\frac{\partial\Delta\beta}{\partial w})_{\{h_{\mathrm{etch}}=154\ nm,\ t_{\mathrm{LN}}=303\ nm,\ \lambda_{\mathrm{pump}}=1580\ nm\}} = -0.485\ \mu m^{-2}, \\ &(\frac{\partial\Delta\beta}{\partial h_{\mathrm{etch}}})_{\{w=850\ nm,\ t_{\mathrm{LN}}=303\ nm,\ \lambda_{\mathrm{pump}}=1580\ nm\}} = 1.842\ \mu m^{-2}, \\ &(\frac{\partial\Delta\beta}{\partial t_{\mathrm{LN}}})_{\{w=850\ nm,\ h_{\mathrm{etch}}=154\ nm,\ \lambda_{\mathrm{pump}}=1580\ nm\}} = -4.018\ \mu m^{-2}. \end{aligned} \tag{2}$$

The calculations reveal that $\Delta\beta$ of the waveguide structure employed in this study is most sensitive to variations in film thickness, which agrees with simulation results and insights from previous investigations in Refs. [1,2,14,15,24]. In addition, according to the general framework developed in Ref. [16], the correlation between QPM spectral fidelity and phase mismatch errors can be approximately fitted through a Lorentzian-like function as:

$$\begin{aligned} F(\sigma L) &= \frac{1}{(1+A(\sigma L)^B)^C} \\ \sigma &\approx |\frac{\partial\Delta\beta}{\partial p}|\Delta p, \end{aligned} \tag{3}$$

where A, B and C are fitted values from Ref. [16] as 0.0054, 2.12, and 0.35 respectively, p stands for a single waveguide parameter (here as w, h_{etch}, and t_{LN}), and Δp is the amplitude of the waveguide geometry variations, reflecting the deviation from the nominal waveguide parameter values. This is obtained under the assumptions that the phase mismatch errors are sufficiently small to be considered as frequency-independent, and they exhibit 1/f noise to account for the long-range correlations arising from the fabrication processes. Using Eq. 3, we further estimated the contribution from each individual waveguide parameter (Δp) to the QPM spectrum infidelity for all four waveguides, and the results are summarized in Table 1. This estimation assumes that the spectrum infidelity is primarily influenced by a single waveguide parameter. The similarity in the calculated variations for each parameter across all four waveguides provides further evidence of the consistent nature of the fabrication variations throughout the entire chip.

TABLE I. Estimated waveguide geometry variation for all four waveguides based on the measured QPM spectra.

Waveguide length	Δw	Δh_{etch}	Δt_{LN}
5 mm	13.16 nm	3.47 nm	1.59 nm
7.5 mm	22.04 nm	5.81 nm	2.66 nm
12.5 mm	20.70 nm	5.46 nm	2.50 nm
15 mm	20.42 nm	5.38 nm	2.47 nm

We conducted precise measurements using atomic force microscopy (AFM) on a twin chip to assess the variations in waveguide width and etching depth along a 15 mm long waveguide. The calculated errors for both parameters were found to be lower than the estimated values mentioned in Table 1, with the measured widths (etching depths) showing a maximum deviation of 10.6 nm (1.9 nm). On the other hand, the estimated variations in film thickness appear more plausible, as such levels of long-range variation can often arise from the thin-film fabrication process (including ion implantation and chemical-mechanical polishing) and are consistent with the labeled thickness uniformity value provided by the wafer vendor. In order to examine the film thickness variations, we conducted spectral reflectance measurements across the entire etched chip, using a thin-film metrology instrument named Filmetrics F-54. To achieve accurate fitting of the measured reflectance at normal incidence, we utilized a dispersive model for the refractive index of MgO-doped TFLN at room temperature[27]. The light source has a spot size of 17 μm, and the measurements were taken with a step size of 200 μm, resulting in the thickness mapping illustrated in Fig. 3(a). It is

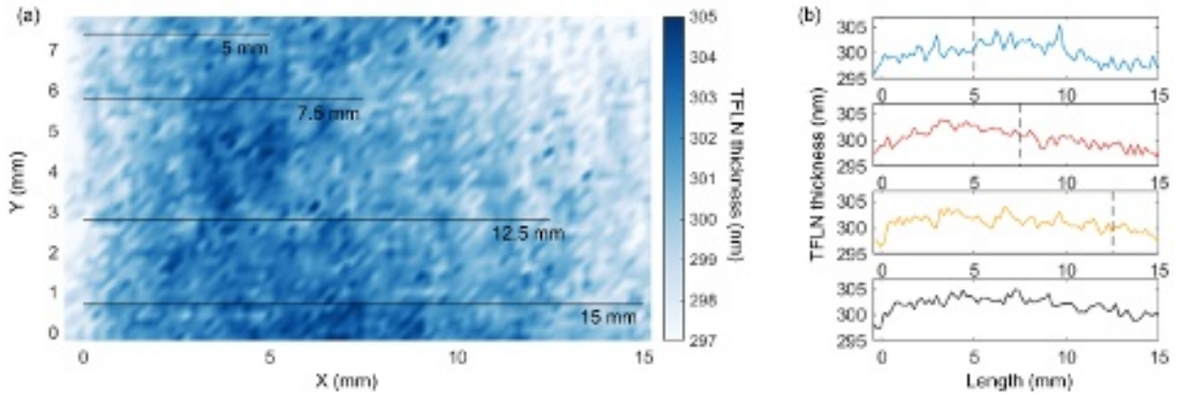

FIG. 3. (a) Measured TFLN film thickness mapping over the entire chip, with the black lines showing the position of PPLN waveguides. (b) Measured TFLN thickness along the waveguides with periodically poled regions of 5 mm (blue), 7.5 mm (red), 12.5 mm (yellow), and 15 mm (black). The black dashed lines indicate the end of the PPLN region for each waveguide.

important to note that, since LN is anisotropic and the UV-light source utilized in the reflectance measurement is unpolarized, the measured film thickness may not be accurate in absolute terms, with a potential constant error across different points of the mapped film. However, for the purpose of this study, our main concern lies in determining the relative thickness variation rather than obtaining the absolute thickness across the chip. Notably, the goodness of fit (GOF) for all the measured points exceeded 97%, indicating the accuracy of the fitting process. It is worth mentioning that this measurement was conducted subsequent to the dry-etching process of the waveguide. Therefore, the plotted thickness values in Fig. 3 represent the raw measured data, augmented by a constant etching depth of 154 nm (measured after the dry etching process). As depicted in Fig. 3(a), it is evident that the film thickness exhibits consistent variations across the entire chip, which aligns with our hypothesis based on the QPM spectrum mappings shown in Fig. 2. Specifically, the thickness gradually increases from the left edge of the chip (the input port of the PPLN) and subsequently decreases towards the right side (the output port of the PPLN). In addition to the overall mapping, Fig. 3(b) provides a detailed plot of the measured TFLN thickness along four specific waveguides with lengths of 5 mm (blue), 7.5 mm (red), 12.5 mm (yellow), and 15 mm (black). The dashed lines in the figure indicate the end of the PPLN regions. Notably, the chip analyzed in this study was obtained from an area near the edge of the wafer. The thickness profile, which exhibits a high-order polynomial trend, observed in this specific chip was not present in subsequent measurements conducted on chips extracted from regions in the center of the wafer.

Utilizing these film thickness values, we numerically calculated the QPM spectrum mapping for all four waveguides, based on the methods described in Refs. [20,28]. To perform this simulation, we calculated the refractive indices and optical mode profiles of the TFLN waveguides using a commercial eigenmode (FDE) solver named Lumerical MODE Solutions. Subsequently, the calculations for the QPM spectrum mappings were conducted in MATLAB using data acquired from Lumerical MODE Solutions. These mappings are presented in Figs. 2(b), (e), (h), and (k). We also depicted the end-point QPM spectra in Figs. 2(c), (f), (i), and (l), overlaid with the curves acquired experimentally. A thorough comparison of these plots highlights the successful reproduction of the main side lobes observed in the measured QPM spectra for all four waveguides. Moreover, the simulations accurately captured the evolution trend evident in the measured QPM spectrum mappings. Several factors may contribute to the observed discrepancies between the measured and simulated mappings in this study. These factors include local variations in waveguide widths and etching depth, which are considered secondary factors here and thus are not included in the numerical calculations. Furthermore, considering the high sensitivity of the spectra to film thickness variations, even slight deviations from the true values, such as the absence of fine features in the captured thickness profile and errors resulting from imperfect measurement accuracy, can contribute to the observed disparities. Taking the 15 mm PPLN waveguide as an example, in Fig. 4, we show that slight local variations in the film thickness profile can provide better alignment to the measured QPM spectra. The optimized film thickness profile, as shown in Fig. 4(a), was obtained using the Particle Swarm Optimization algorithm, where upper and lower thickness constraints were set at 305 nm and 295 nm. The aim of this optimization process was to reproduce the QPM spectra at various positions along the waveguide, as displayed in Fig. 4(c). Note that the difference between the optimized thickness profile and the raw data can be introduced by waveguide parameters other than film thickness, such as waveguide width and etching depth. As for the 12.5 mm long waveguide, we could achieve a better matching with the measured QPM spectrum mapping (shown in Fig. 2(h)) by adding 2 nm to the poling period, shifting the whole spectrum to longer wavelengths, though the alignment with the end-point QPM spectrum would be compromised. We emphasize that the primary goal of this work is not to achieve a perfect replication of the measured QPM spectrum mapping. Instead, the focus is on experimentally identifying the main sources (waveguide

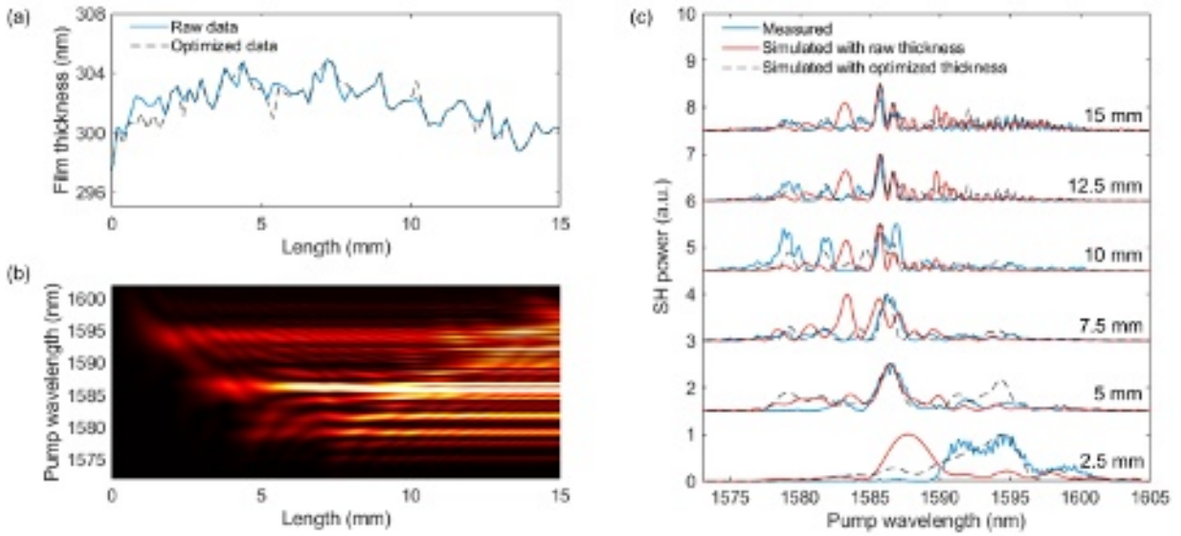

FIG. 4. (a) Comparison of the measured and optimized film thickness profile for the 15 mm long waveguide. (b) Simulated QPM spectrum mapping using the optimized thickness profile. (c) QPM spectra at different locations along the waveguide obtained through the experiment (solid blue curve), simulations with raw thickness profile (solid red curve), as well as simulations with optimized thickness profile (dashed black curve).

sections and parameters) responsible for the spectral imperfections. Nevertheless, the close agreement between the simulated and measured QPM spectra provides strong evidence supporting the hypothesis that the observed imperfections primarily originate from variations in the film thickness along the waveguiding region.

IV. CONCLUSION AND DISCUSSION

In conclusion, our study introduces a simple yet effective non-destructive optical diagnostic method for assessing imperfections in QPM spectra from thin-film PPLN waveguides. This approach allows for the extraction of QPM spectra at any position along the waveguide without the need for physically dicing the waveguides. By comparing the measured spectrum mappings with ideal ones, we can accurately identify specific regions contributing to unwanted distortions in the QPM spectra, providing crucial insights into the sources of these spectral imperfections. Using this approach, we obtained QPM spectrum mappings from four fabricated thin-film PPLN waveguides with lengths of 5 mm, 7.5 mm, 12.5 mm, and 15 mm. Based on these mappings, we identified variations in TFLN thickness along the waveguide as the primary source of the observed spectral imperfections. Moreover, we replicated the main features of the measured QPM mappings using film thickness data obtained from the spectral reflectance measurements. The strong alignment between the simulated and measured mappings serves to validate the efficacy of the introduced diagnostic technique.

There are several potential avenues for improving the fidelity of QPM spectra. One straightforward approach is to fabricate PPLN waveguides in an area close to the center of the LNOI wafer, where the film thickness is expected to be more uniform and exhibit a reduced variation trend observed in this study. Another promising strategy involves designing waveguide structures that are less sensitive to thickness variations, as explored in simulations detailed in Ref. [14], which may come at the cost of reduced conversion efficiency. SHG devices designed following this concept have been demonstrated experimentally in a recent study[24]. Additionally, obtaining a detailed TFLN thickness mapping prior to waveguide fabrication and compensating for thickness variations through adjustments in other waveguide parameters such as poling period and waveguide width is another viable option. It is also possible to design folded waveguides that possess a smaller area with more uniform film thickness[29], although this would require additional components to control the accumulated phase mismatch in the curved waveguides.

Taken together, our research facilitates the experimental characterization of the sources of imperfections in QPM spectra originating from thin-film PPLN waveguides and complements the numerical studies reported previously[14,15,23,24]. The integration of experimental findings with numerical simulations provides helpful insights into the path toward the development of long thin-film PPLN devices with enhanced overall conversion efficiency. These insights hold great potential for benefiting applications in both classical and quantum communication domains, opening up new possibilities for enhanced performance and functionality.

Note: While preparing this manuscript, we became aware of a related study (Ref. [30]) reporting the demonstration of long thin-film PPLN devices achieved by adapting the poling period of TFLN to compensate for film thickness variations.

ACKNOWLEDGMENTS

The authors would like to acknowledge the Research Grants Council, University Grants Committee (CityU 11204820, N_CityU113/20) for funding this work. Jie Zhao would like to thank Haowen Ren, Yanqi Luo, and Yang Li for their valuable discussions and assistance in the fabrication process.

AUTHOR DECLARATIONS

Conflict of Interest

The authors have no conflicts to disclose.

DATA AVAILABILITY STATEMENT

Data underlying the results presented in this paper are not publicly available at this time but may be obtained from the corresponding author upon reasonable request.

REFERENCES

[1]C. Wang, C. Langrock, A. Marandi, M. Jankowski, M. Zhang, B. Desiatov, M. M. Fejer, and M. Lončar, "Ultrahigh-efficiency wavelength conversion in nanophotonic periodically poled lithium niobate waveguides," Optica **5**, 1438–1441 (2018).

[2]L. Chang, Y. Li, N. Volet, L. Wang, J. Peters, and J. E. Bowers, "Thin film wavelength converters for photonic integrated circuits," Optica **3**, 531–535 (2016).

[3]A. Boes, L. Chang, M. Knoerzer, T. G. Nguyen, J. D. Peters, J. E. Bowers, and A. Mitchell, "Improved second harmonic performance in periodically poled LNOI waveguides through engineering of lateral leakage," Opt. Express **27**, 23919–23928 (2019).

[4]J. Zhao, M. Rüsing, U. A. Javid, J. Ling, M. Li, Q. Lin, and S. Mookherjea, "Shallow-etched thin-film lithium niobate waveguides for highly-efficient second-harmonic generation," Opt. Express **28**, 19669–19682 (2020).

[5]A. Rao, K. Abdelsalam, T. Sjaardema, A. Honardoost, G. F. Camacho-Gonzalez, and S. Fathpour,, "Actively-monitored periodic-poling in thin-film lithium niobate photonic waveguides with ultrahigh nonlinear conversion efficiency of 4600 $\%W^{-1}cm^{-2}$," Opt. Express **27**, 25920–25930 (2019).

[6]X. Liu, S. Gao, C. Zhang, Y. Pan, R. Ma, X. Zhang, L. Liu, Z. Xie, S. Zhu, S. Yu, and X. Cai, "Ultra-broadband and low-loss edge coupler for highly efficient second harmonic generation in thin-film lithium niobate," Adv. Photon. Nexus **1**, 016001 (2022).

[7]J. Lu, J. B. Surya, X. Liu, A. W. Bruch, Z. Gong, Y. Xu, and H. X. Tang, "Periodically poled thin-film lithium niobate microring resonators with a second-harmonic generation efficiency of 250,000%/W," Optica **6**, 1455–1460 (2019).

[8]J.-Y. Chen, Y. M. Sua, Z.-H. Ma, C. Tang, Z. Li, and Y.-P. Huang, "Ultra-efficient frequency conversion in quasi- phase-matched lithium niobate microrings," Optica **6**, 1244–1245 (2019).

[9]J. Zhao, C. Ma, M. Rüsing, and S. Mookherjea, "High Quality Entangled Photon Pair Generation in Periodically Poled Thin-Film Lithium Niobate Waveguides," Phys. Rev. Lett. **124**, 163603 (2020).

[10]Z. Ma, J.-Y. Chen, Z. Li, C. Tang, Y. M. Sua, H. Fan, and Y.-P. Huang, "Ultrabright Quantum Photon Sources on Chip," Phys. Rev. Lett. **125**, 263602 (2020).

[11]L. Ledezma, R. Sekine, Q. Guo, R. Nehra, S. Jahani, and A. Marandi, "Intense optical parametric amplification in dispersion engineered nanophotonic lithium niobate waveguides," Optica **9**, 303–308 (2022).

[12]K. Abdelsalam, T. Li, J. B. Khurgin, and S. Fathpour, "Linear isolators using wavelength conversion," Optica **7**, 209–213 (2020).

[13]Q. Guo, R. Sekine, L. Ledezma, R. Nehra, D. J. Dean, A. Roy, R. M. Gray, S. Jahani, and A. Marandi, "Femtojoule, femtosecond all-optical switching in lithium niobate nanophotonics," Nat. Photonics **16**, 625–631 (2022).

[14]P. S. Kuo, "Noncritical phasematching behavior in thin-film lithium niobate frequency converters," Opt. Lett. **47**, 54–57 (2022).

[15]X.-H. Tian, W. Zhou, K.-Q. Ren, C. Zhang, X. Liu, G.-T. Xue, J.-C. Duan, X. Cai, X. Hu, Y.-X. Gong, Z. Xie, and S.-N. Zhu, "Effect of dimension variation for second-harmonic generation in lithium niobate on insulator waveguide [Invited]," Chin. Opt. Lett. **19**, 060015 (2021).

[16]M. Santandrea, M. Stefszky, and C. Silberhorn, "General framework for the analysis of imperfections in nonlinear systems," Opt. Lett. **44**, 5398 (2019).

[17]T. Umeki, O. Tadanaga, and M. Asobe "Highly efficient wavelength converter using direct-bonded PPZnLN ridge waveguide," IEEE J. Quantum Electron. **46**, 1206–1213 (2010).

[18]K. R. Parameswaran, R. K. Route, J. R. Kurz, R.V. Roussev, M. M. Fejer, and M. Fujimura "Highly efficient second-harmonic generation in buried waveguides formed by annealed and reverse proton exchange in periodically poled lithium niobate," Opt. Lett. **27**, 179–181 (2002).

[19]M. Santandrea, M. Stefszky, G. Roeland, and C. Silberhorn, "Characterisation of fabrication inhomogeneities in Ti: $LiNbO_3$ waveguides," New J. Phys. **21**, 123005 (2019).

[20]M. Santandrea, M. Stefszky, V. Ansari, and C. Silberhorn, "Fabrication limits of waveguides in nonlinear crystals and their impact on quantum optics applications," New J. Phys. **21**, 033038 (2019).

[21]A. C. Gray, S. A. Berry, L. G. Carpenter, J. C. Gates, P. G. Smith, and C. B. Gawith, "Investigation of PPLN Waveguide Uniformity via Second Harmonic Generation Spectra," IEEE Photonics Technol. Lett. **32**, 63–66 (2020).

[22]D. Chang, C. Langrock, Y.-W. Lin, C. R. Phillips, C. V. Bennett, and M. M. Fejer, "Complex-transfer-function analysis of optical-frequency converters," Opt. Lett. **39**, 5106–5109 (2014).

[23]G.-T. Xue, X.-H. Tian, C. Zhang, Z. Xie, P. Xu, Y.-X. Gong, and S.-N. Zhu, "Effect of thickness variations of lithium niobate on insulator waveguide on the frequency spectrum of spontaneous parametric down-conversion," Chin. Phys. B **30**, 110313 (2022).

[24]E. Hwang, N. Harper, R. Sekine, L. Ledezma, A. Marandi, and S. Cushing, "Tunable and efficient ultraviolet generation in nanophotonic lithium niobate," Opt. Lett. **48**, 3917–3920 (2023).

[25]J. Zhao, M. Rüsing, M. Roeper, L. M. Eng, and S. Mookherjea, "Poling thin-film x-cut lithium niobate for quasi-phase matching with sub-micrometer periodicity," J. Appl. Phys. **127**, 193104 (2020).

[26]M. M. Fejer, D. H. Jundt, R. L. Byer, and G. A. Magel, "Quasi-Phase-Matched Second Harmonic Generation: Tuning and Tolerances," IEEE J. Quantum Electron. **28**, 2631–2654 (1992).

[27]O. Gayer, Z. Sacks, E. Galun, and A. Arie, "Temperature and wavelength dependent refractive index equations for MgO-doped congruent and stoichiometric $LiNbO_3$," Appl. Phys. B **91**, 343–348 (2008).

[28]S. Helmfrid, G. Arvidsson, and J. Webjorn, "Influence of various imperfections on the conversion efficiency of second-harmonic generation in quasi-phase-matching lithium niobate waveguides," J. Opt. Soc. Am. B **10**, 222–229 (1992).

[29]P. O. Weigel and S. Mookherjea, "Design of folded hybrid silicon carbide-lithium niobate waveguides for efficient second-harmonic generation," J. Opt. Soc. Am. B **35**, 593–600 (2018).

[30]P.-K. Chen, I. Briggs, C. Cui, L. Zhang, M. Shah, and L. Fan, "Adapted poling to break the nonlinear efficiency limit in nanophotonic lithium niobate waveguides," arXiv preprint arXiv:2307.11671 (2023).

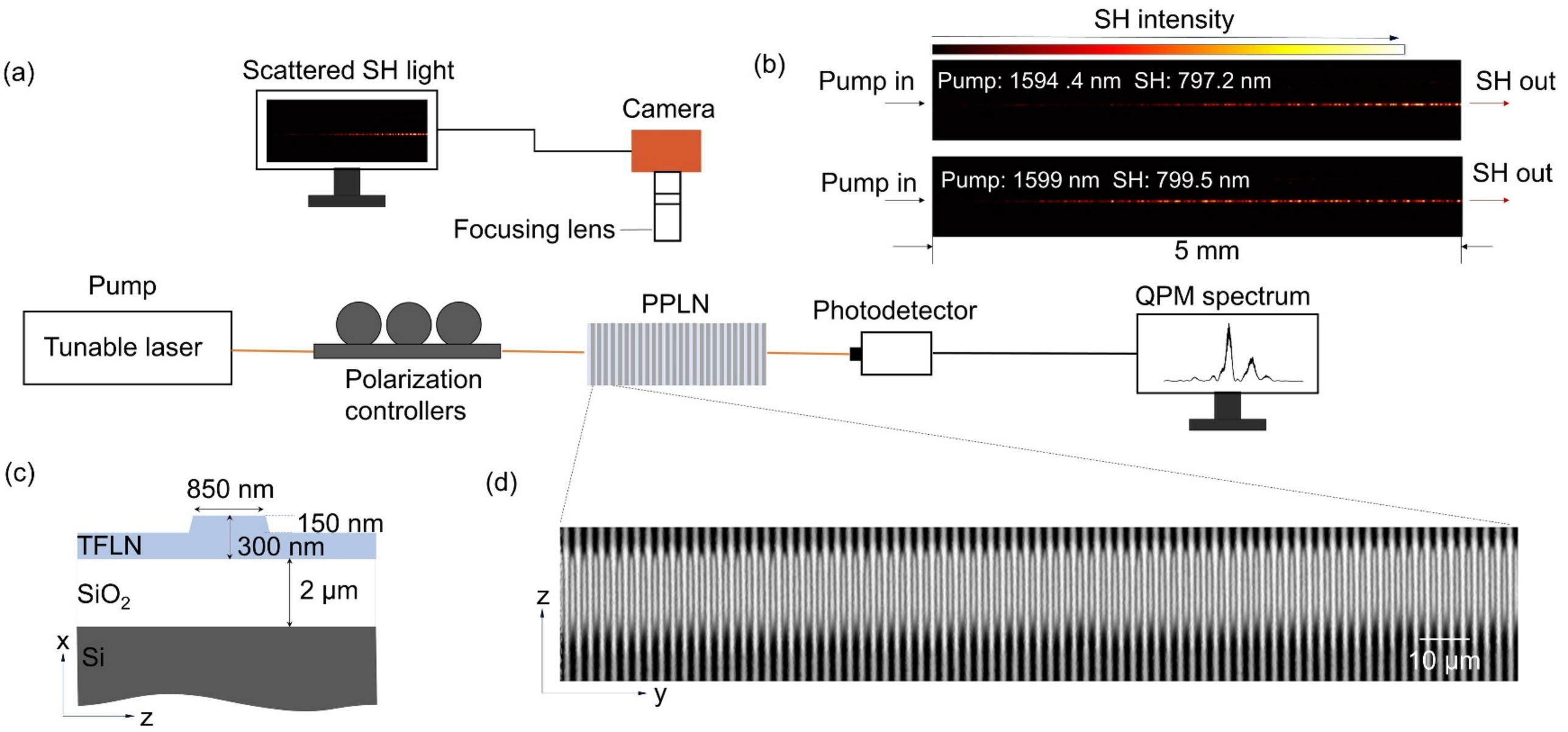
(a)
Scattered SH light
Camera
Focusing lens
(b)
SH intensity
Pump in
Pump: 1594 .4 nm SH: 797.2 nm
SH out
Pump in
Pump: 1599 nm SH: 799.5 nm
SH out
5 mm
Pump
Tunable laser
Polarization controllers
PPLN
Photodetector
QPM spectrum
(c)
850 nm
150 nm
TFLN
300 nm
SiO_2
2 μm
Si
x
z
(d)
z
y
10 μm

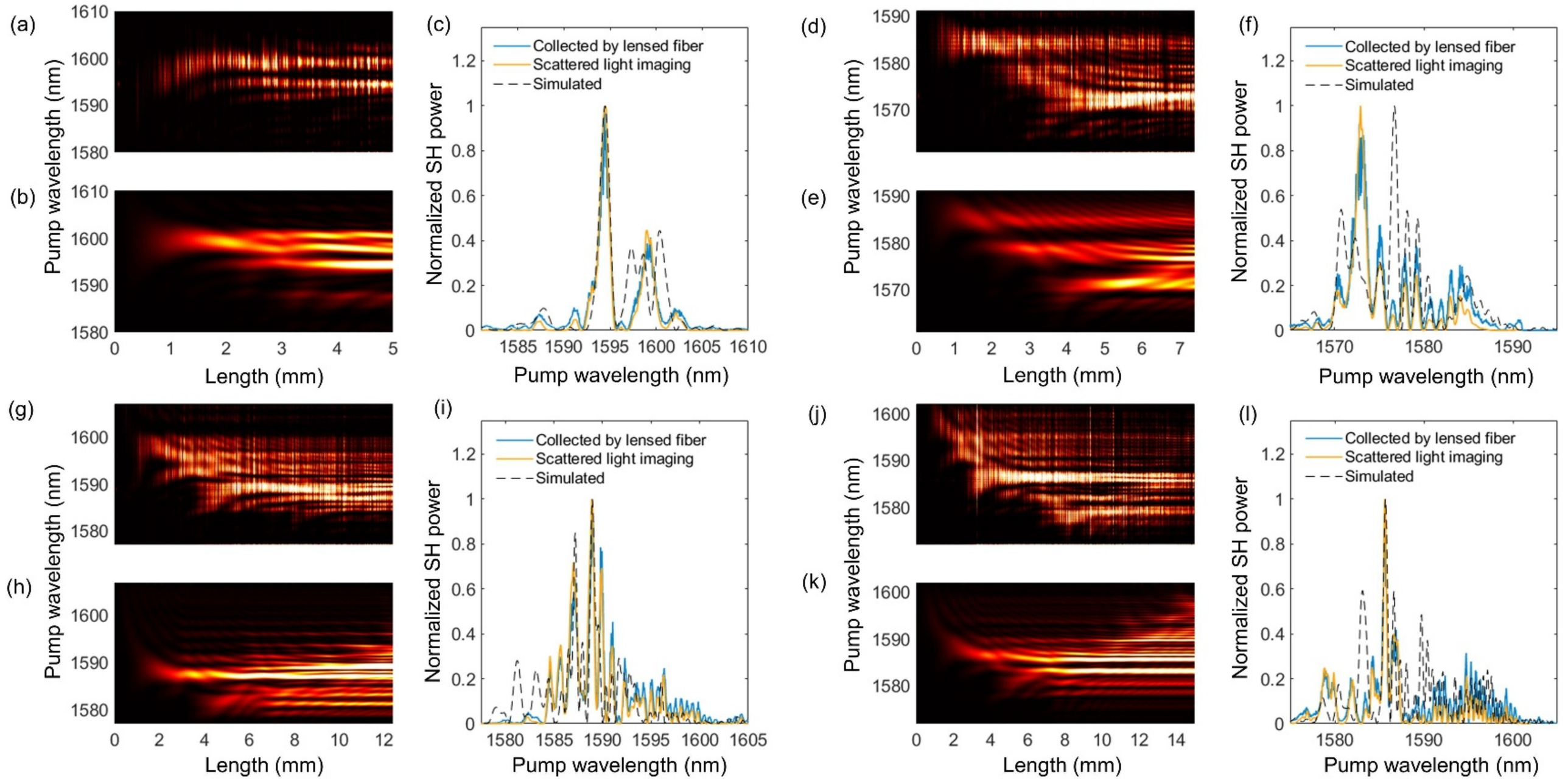
(a)
(b)
(c)
(d)
(e)
(f)
(g)
(h)
(i)
(j)
(k)
(l)
Pump wavelength (nm)
Length (mm)
Normalized SH power
Pump wavelength (nm)
Collected by lensed fiber
Scattered light imaging
Simulated

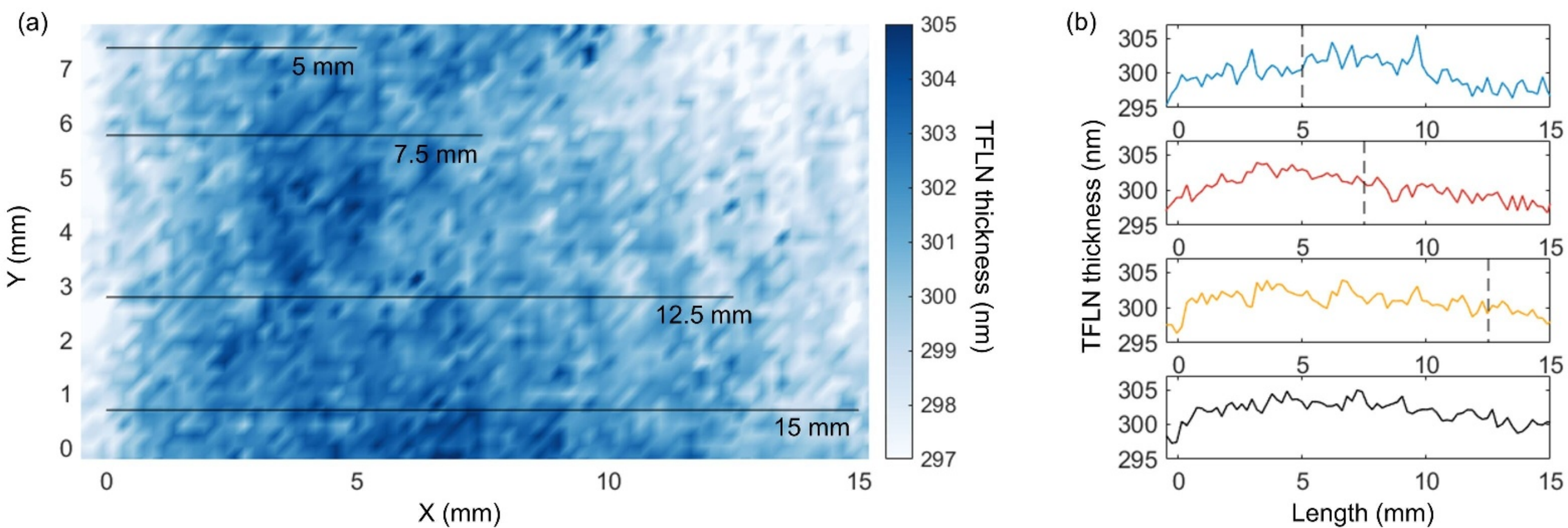
(a)
5 mm
7.5 mm
12.5 mm
15 mm
Y (mm)
X (mm)
TFLN thickness (nm)
(b)
TFLN thickness (nm)
Length (mm)

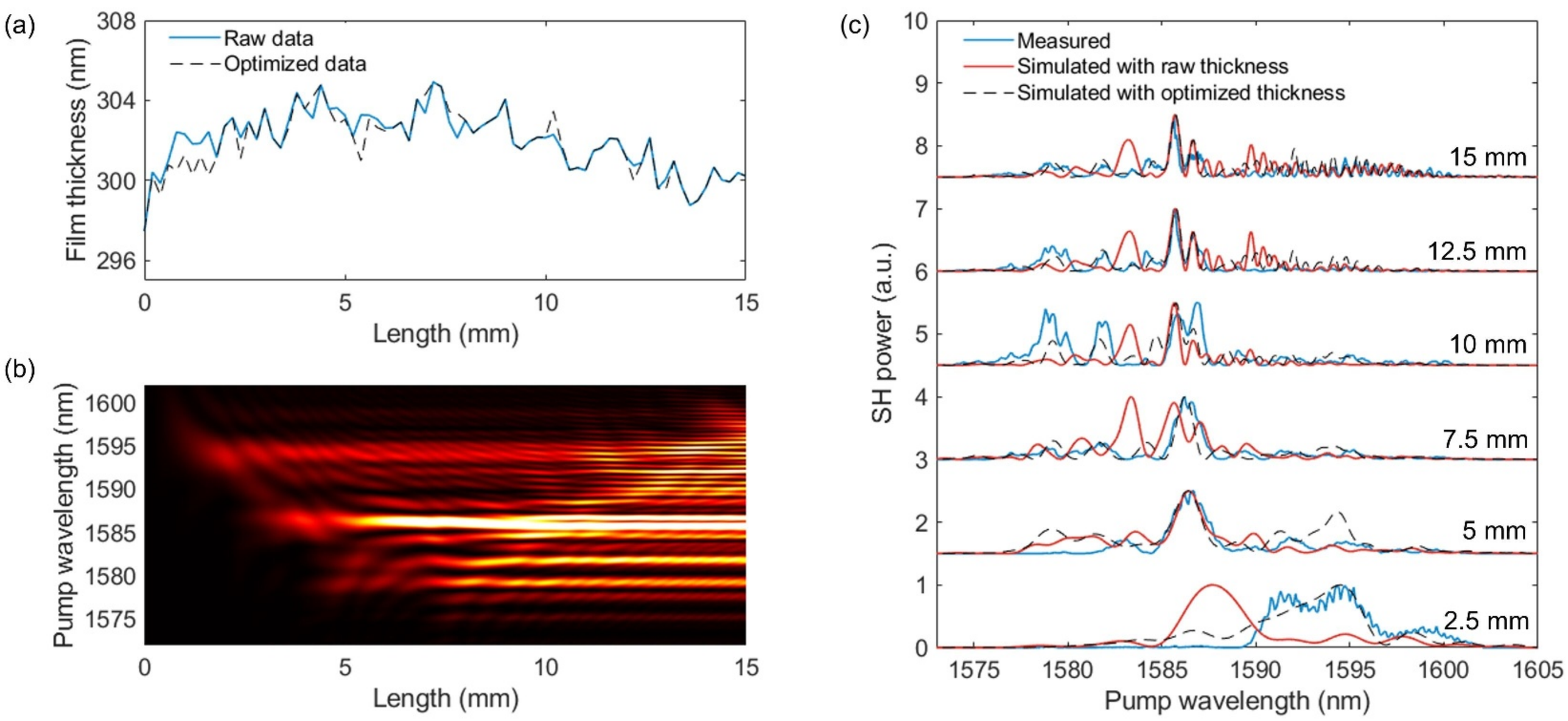
(a)
Raw data
Optimized data
Film thickness (nm)
308
304
300
296
0
5
10
15
Length (mm)
(b)
Pump wavelength (nm)
1600
1595
1590
1585
1580
1575
0
5
10
15
Length (mm)
(c)
Measured
Simulated with raw thickness
Simulated with optimized thickness
SH power (a.u.)
10
9
8
7
6
5
4
3
2
1
0
15 mm
12.5 mm
10 mm
7.5 mm
5 mm
2.5 mm
1575
1580
1585
1590
1595
1600
1605
Pump wavelength (nm)